AIChE

Rotating Corrugated Photoreactor Design: Experimental and Computational Analysis of TiO_2-Based Photocatalysis

Adam A. Donaldson
Dept. of Process Engineering and Applied Science, Dalhousie University, PO Box 15000, Halifax, Nova Scotia,
Canada B3H 4R2

Alice Ye, Joanne Gamage McEvoy, and Zisheng Zhang
Dept. of Chemical and Biological Engineering, University of Ottawa, 161 Louis Pasteur Street, Ottawa, Canada K1N 6N5

DOI 10.1002/aic.13829

A TiO_2-coated rotating corrugated reactor is experimentally characterized and simulated for ultraviolet (UV)-based photo degradation of methylene blue (MB). Using degradation kinetics derived from flat-plate experiments and finite-element discrete-ordinate models simulating spatially and temporally varying radiation patterns from a UV-lamp array, the simulated reactor performance is experimentally validated and extended to explore the impact of geometry variations. Mass-transfer limitations between the corrugated surface and the reservoir bulk are identified as a determining factor in the degradation rate of MB. Optimization studies suggest minimizing the corrugation half-angle to improve reactor performance for a given area, increasing the number of corrugations rather than the corrugation depth subject to practical limitations arising from undesirable bubble formation at small aperture widths. Given the relevance of mass transfer to this system, future work is needed to elucidate the experimental impact of reservoir volume and geometry while validating the use of flat-plate correlations for mass transfer.
AIChE J, 59: 560–570, 2013
Keywords: photochemical reactions, reactor analysis, complex radiation simulation, surface chemistry/physics, environmental engineering

Introduction

Ultraviolet (UV) radiation-based photocatalytic reactions involving both gases and liquids are frequently reported in the literature for applications in industrial sectors requiring wastewater treatment.[1] Many of these processes involve the photoexcitation of either a reactant or catalyst as a limiting step governing reaction kinetics, whereby the UV absorption profile within a reactor geometry for a given light source is a determining factor in the system's performance and optimum configuration. A number of radiative transfer models exist for predicting the UV absorption profile for absorbing, reacting, and scattering media,[2] based on one of the three computational approaches: Monte Carlo,[3,4] discrete ordinate (DO) models,[5,6] and a conservative finite-volume variant of the DO model.[7,8] Previous work on a computationally robust DO implementation for corrugated reactor geometries has enabled the determination of local area-specific rates of energy absorption (LASREA) for practical reactor configurations illuminated by complex light sources,[9–12] which can be coupled with local mass-transfer rates to optimize reacting systems.[13] In this work, the developed implementation is used to analyze the performance of TiO_2-catalyzed photo degradation of methylene blue (MB) solution in a novel rotating corrugated reactor system.

UV-based rotating corrugated photocatalytic reactors have recently been considered for applications involving gravity-driven flow or batch systems where chemical-based disinfection methods are less desirable.[14] Partial insertion of the reactor geometry into a flowing media induces constant rotation that continuously refreshes the fluid media at the catalytic surface. The thin film created during rotation has minimal mass-transfer limitations for both the contaminant and oxygen needed for photo degradation. The reactor configuration also offers a high-surface area-to-volume ratio and catalyst loading, allowing for extended operation before complete deactivation of the catalytic surface. Analysis of the rotating corrugated reactor system is complicated by the transient radiation pattern within each corrugation and spatial variations in the local film concentrations. A coupled experimental and computational analysis was thus completed to characterize the rotating reactor system and to identify potential optimization strategies for second-generation reactor design.

Equipment and Materials

The photocatalytic degradation of dilute MB solutions (8–12 mg/L) was performed in a custom-made UV exposure system consisting of an array of 20 tightly packed 25 W T8 linear fluorescent black lights (F25T8/BL) driven by five

---

Correspondence concerning this article should be addressed to A. A. Donaldson at adam.donaldson@dal.ca, or Z. Zhang at jason.zhang@uottawa.ca.

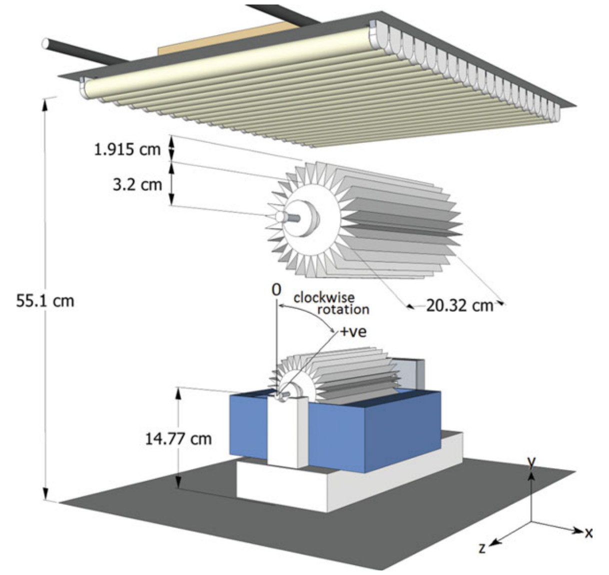

Figure 1. Corrugated reactor geometry (N_c = 28) and positioning relative to lamp array.

[Color figure can be viewed in the online issue, which is available at wileyonlinelibrary.com.]

Sylvania Quicktronic F32T8 ballasts (Figure 1). The center-to-center spacing between bulbs was approximately 2.84 ± 0.05 cm, with each bulb having a diameter of 2.54 cm and an emitting length of 45.16 cm. The bottom edge of the lamp array was located 55.1 cm above the counter on which it was mounted. With a specific lamp power exceeding 693.75 W/m^2, the equivalent UV index for near-lamp exposure exceeded 39 after accounting for the McKinlay–Diffey Erythema action spectrum and lamp spectral distribution. Based on simulated and measured irradiance below the lamps, exposure in the working region equated to an approximate UV index of 10, corresponding to high/extreme risk. A ventilated aluminum light box enclosure was thus constructed around the lamp array for operator safety and heat dissipation, with an external liquid recirculation loop for fluid sampling (6.35 mm internal tube diameter, 2 m length). The MB concentration in the collected samples was determined from the solution's light absorbance at 665 nm. UV intensity at different points within the light box was measured using a UVX digital UV intensity meter (Cole-Parmer, RK-97651-10) equipped with a 365-nm sensor (Cole-Parmer, RK-97651-22).

Batch experiments were performed using circular sand-blasted stainless-steel plates (d_{plate} = 8.14 ± 0.064 cm) coated with TiO_2 (Degussa Aeroxide TiO_2 P25) and placed in a beaker containing 250 mL of dilute MB solution. The MB solution was pumped through the external recirculation and sampling loop at a rate of 0.59 L/min using a peristaltic pump. This recirculation induced significant mixing within the beaker without the use of magnetic stirring (thereby avoiding damage to the TiO_2 coating), while also minimizing time delays introduced during remote sampling. During experiments, the beaker was positioned below the center of the lamp array, and was elevated such that the vertical distance between the coated plate and bottom of the lamp was 31.9 cm. The TiO_2 coating was applied to each plate via mechanical brushing of a 180-g TiO_2/L 3:1(volume) water:methanol solution onto the surface followed by 5 h of annealing at 250°C. This method consistently resulted in the deposition of 36 to 40 mg of TiO_2 onto the surface of the plate.

Rotating corrugated reactor experiments were performed using a stainless steel drum surrounded by $N_c = 28$ corrugations, each having an approximate depth, corrugation half-angle, and length of 1.915 cm, 6.43°, and 20.32 cm, respectively (Figure 1). The fold of the corrugation was located approximately 3.2 cm from the drum's center of rotation, which was positioned 14.77 cm above the light-box counter when in operation (i.e., 40.35 cm below the base of the lamp array). The drum was coupled to a DC motor, with the rotation rate controlled by the set voltage of the connected power supply. Similar to the flat-plate experiments, a 180-g TiO_2/L 3:1(volume) water:methanol solution was brushed onto the surface before annealing at 250°C for 5 h.

Computational Methodology

The current system uses initial MB concentrations on the order of 10 mg/L and LASREAs up to 145.6 W/m^2, values for which the rate of degradation will be dependent on both MB diffusion and energy incidence. For the purpose of this analysis, a Langmuir–Hinshelwood rate equation for MB degradation was assumed with an additional modifier for radiation intensity. Assuming the applicability of Fick's law for describing mass transfer from the bulk to the surface and negligible variations in dissolved oxygen levels over the course of the experiments, the rate equation can be simplified to

$$-r_{\mathrm{MB}} = \frac{k_0 C_{\mathrm{MB}}}{(1+K_1 C_{\mathrm{MB}})}\left(\frac{q_i}{q_0}\right)^{0.5}, \tag{1}$$

$$C_{\mathrm{MB}} = C_{\mathrm{bulk}} + \frac{\delta}{D_{\mathrm{MB}}} r_{\mathrm{MB}} = \frac{-B+\sqrt{B^2+4K_1 C_{\mathrm{bulk}}}}{2K_1}, \tag{2}$$

where k_0 [(m^3 solution)/(m^2 area)^1/min^1] and K_1 (m^3/g^1) are fitted coefficients, C_{MB} is the concentration of MB at the surface (g/m^3), C_{bulk} is the concentration of MB in the bulk (g/m^3), q_i is the spatially varying LASREA (W/m), $q_0 = 1$ (W/m), δ is the thickness of the boundary layer across which diffusion occurs (m), D_{MB} is the diffusivity of MB in water (assumed to be 3×10^{-8} m^2/min),[15] and $B = 1 + k_0\,(\delta/D_{\mathrm{MB}})(q_i/q_0)^{0.5} - K_1 C_{\mathrm{bulk}}$. This expression is similar in form to that applied previously for 4-chlorophenol in a corrugated reactor system with comparable initial concentrations and LASREA magnitudes.[16,17]

Although previous MB degradation literature has assumed diffusion lengths of $\delta \sim 100$ μm,[15] this value exceeds typical film thicknesses on the corrugated system (14.5 to 49.4 μm, depending on rotation rate and radial position). The external flow recirculation loop used in the flat-plate experiments discharged across the surface of the plate at a velocity of 0.31 m/s, creating significant mixing within the reservoir. Assuming a flat-plate length equivalent to the diameter of the plate (0.0814 m) and physical properties comparable to water, an equivalent film thickness of 40 μm was applied[18] during regression of the kinetic data. For the corrugated reactor, δ was assumed equivalent to the local film thickness, δ_i, from Eq. 20.

Flat-plate experiments were performed to determine the values of k_0 and K_1, assuming a quadratic relationship between catalyst deactivation and total MB decomposed, D (g MB/m^2). The LASREA, q_i, used in Eq. 1 for the flat plates was simulated via the methodology described in the following sections, thus, decoupling the fitted coefficients from the radiation distribution so that the kinetic expression could be extended to the rotating corrugated reactor geometry. Determining the LASREA within the corrugated reactors required a number of additional considerations due to the impact of photon recapture, the three-dimension (3-D) nature of the geometry, and the fact that the corrugation's orientation varied as the drum rotated. Defining the rotation of the reactor as the degrees clockwise rotation of the corrugation fold from the vertical (Figure 1), the incident energy and LASREA were simulated at rotations from 0° to 100°. At each rotation, the 2-D profile of the corrugated geometry was discretized into 1000 elements and the direct lamp incidence determined at 21 equal-spaced locations along the extruded reactor length. These incident energy profiles often exhibited minimal variations in the extruded direction and were thus averaged using trapezoidal integration to obtain a representative incident energy profile. This profile was subsequently used to determine the LASREA per W/m^2 specific lamp emission rate for spectral absorption coefficients ranging from 0 to 100%. The emission spectra of the lamp was then used to determine the specific lamp emission rate at different wavelengths, which was combined with the spectral absorption coefficient of TiO_2 to determine the total LASREA at each wavelength. The total LASREA at a given position on the corrugation, q_i, was then taken as the sum of the total LASREA at each wavelength within the spectrum modeled (300 to 580 nm).

Direct incident energy distribution

The conservative finite-element DO method by which the incident energy and LASREA are calculated for a given surface illuminated by a complex light source has been described previously[13] and will only be discussed briefly here within the context of this specific system and modifications made to account for liquid film effects. The local LASREA profile, q_i, is the combined energy absorbed directly from the light source and from photon recapture. In this study, the direct incidence, I_i (W/m^2), at different points on the flat or corrugated surface, $\vec{P}_i$, from a fully discretized array of 20 lamps (S_{Light}, ~3.6 million surface elements of area dA_j) was determined from the following equation

$$I_i = \sum_{S_{\text{Light}}} T_{i,j} F_{i,j} W_{\text{light}}\, dA_j, \tag{3}$$

where W_{light} is the specific emission rate (W/m^2) at any given wavelength within the lamp's spectrum, $F_{i,j}$ is the emission factor for light emitted from point $\vec{P}_j = (x_j, y_j, z_j)$ at the center of computational element j on the light's surface and received at $\vec{P}_i$ on the reactor surface, and $T_{i,j}$ is the transmittance through the thin film on the surface of the geometry. As the light source and reactor geometry are typically far away, a simplified expression approximating the solid angle can be used for $F_{i,j}$ based on the unit normal vectors, $\vec{n}_i$ and $\vec{n}_j$, at points $\vec{P}_i$ and $\vec{P}_j$

$$F_{i,j} = -\frac{1}{\pi}\left(\frac{\vec{n}_i \cdot \vec{v}_{i-j}}{\left|\vec{v}_{i-j}\right|^3}\right)\left(\frac{\vec{n}_j \cdot \vec{v}_{i-j}}{\left|\vec{v}_{i-j}\right|}\right), \tag{4}$$

$$\vec{v}_{i-j} = \vec{P}_i - \vec{P}_j. \tag{5}$$

The transmittance through a thin film on the surface of the geometry, $T_{i,j}$, can be approximated using the Fresnel equations for nonpolarized light, assuming refractory indexes of 1 for air and 1.33 for the MB solution

$$\theta_i = \cos^{-1}\left[-\frac{\vec{n}_i \cdot \vec{v}_{i-j}}{\left|\vec{v}_{i-j}\right|}\right], \tag{6}$$

$$R_{S,i,j} = \left(\cos\theta_i - 1.33\sqrt{1-\left(\frac{\sin\theta_i}{1.33}\right)^2}\right)^2 \times \left(\cos\theta_i + 1.33\sqrt{1-\left(\frac{\sin\theta_i}{1.33}\right)^2}\right)^{-2}, \tag{7}$$

$$R_{P,i,j} = \left(\sqrt{1-\left(\frac{\sin\theta_i}{1.33}\right)^2} - 1.33\cos\theta_i\right)^2 \times \left(\sqrt{1-\left(\frac{\sin\theta_i}{1.33}\right)^2} + 1.33\cos\theta_i\right)^{-2}, \tag{8}$$

$$T_{i,j} = 1 - \frac{R_{S,i,j} + R_{P,i,j}}{2}. \tag{9}$$

Note that for the flat-plate experiments, $T_{i,j}$ was assumed equal to 1. For the corrugated reactor experiments, reflections were assumed to diffuse in nature and the effects of the thin film on the diffuse emission pattern from both the MB solution interface and catalyst surface were neglected. In reality, internal reflection within the thin film would increase photon recapture while the intensity of diffuse emissions from the catalyst surface would be reduced at increasing angles from the surface normal. Based on these assumptions, the diffuse emissions resulting from liquid film reflection at point P_i on the reactor surface can be calculated as

$$E_{R,i} = \sum_{S_{\text{Light}}} \left(1 - T_{i,j}\right) F_{i,j} W_{\text{light}}\, dA_j. \tag{10}$$

In determining I_i at each point on the reactor surface, only those lamp elements which would illuminate the surface after accounting for obstructions from the reactor aperture and lamp array configuration were considered (Figure 2). The absorbed energy from direct illumination, $q_{L,i}$, is subsequently determined as

$$q_{L,i} = a(\lambda) I_i, \tag{11}$$

where the spectral absorption coefficient of the TiO_2 film, $a(\lambda)$, at wavelength, λ (nm), is defined as the ratio of absorbed energy to incident energy. In previous work,[9,13] $a(\lambda)$ was specified from a numerical fit of the UV absorption spectra reported by Crittenden et al.[19]

$$a(\lambda) = 0.5 - 0.5\tanh\left(\frac{\lambda - 355.66}{12.743}\right). \tag{12}$$

More recent literature for P25-TiO_2 would suggest that Eq. 12 represents a conservative estimate of the fraction of incident energy absorbed at higher wavelengths in the UV spectra.[20,21]

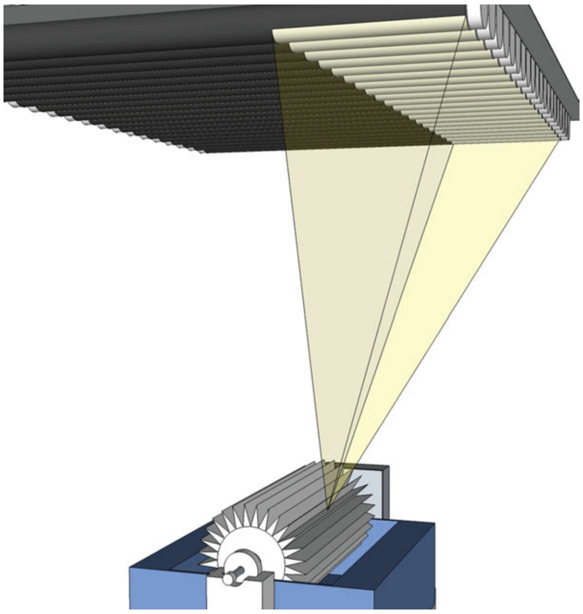

Figure 2. Portion of light surface discretized after accounting for obstructions from aperture and lamp configuration for a typical point on the corrugated reactor surface.

[Color figure can be viewed in the online issue, which is available at wileyonlinelibrary.com.]

For the 9:1 anatase:rutile composition used here, $a(\lambda)$ is more accurately described as

$$a(\lambda) = 1 - 10^{-0.8[1-\tanh((\lambda-352)/35)]}. \tag{13}$$

Note that while Eq. 13 may overestimate the fraction of incident energy absorbed by P25-TiO_2 at wavelengths above 395 nm, the relatively low-lamp emissions at these wavelengths (Figure 3) would limit the net impact on the simulated LASREA reported here.

For the flat-plate reactor, film effects and photon recapture were neglected resulting in $q_i = q_{L,i}$. For the corrugated reactor, the additional effects of photon recapture must be determined.

LASREA per W/m² determination for a(*λ*)

Incident energy from the lamp which is not transmitted through the liquid film or directly absorbed by the catalyst surface is subsequently treated as a diffuse emission from the surface of the reactor geometry, $E_{n,j}$, contributing to the energy absorbed from photon recapture, $q_{R,i}$. $E_{n,j}$ gradually decreases with the number of reflections (subscript n) until subsequent contributions become negligible. For $n = 1$, $E_{1,j}$ is the initial reflection of direct incidence from the lamp at point P_j on the reactor surface [combining I_j (Eq. 3) and $E_{R,j}$ (Eq. 10)], and $I_{1,i}$ is the resulting incidence at some other receiving point, P_i, on the reactor surface

$$E_{1,j} = [1 - a(\lambda)]I_j + E_{R,j}. \tag{14}$$

For subsequent reflections, $E_{n+1,j}$ is determined from $I_{n,j}$ (Eq. 16) and $E_{R,n,j}$ (Eq. 17)

$$E_{n+1,j} = [1 - a(\lambda)]I_{n,j} + E_{R,n,j}. \tag{15}$$

The incidence from reflection n, $I_{n,i}$, at point, $\vec{P}_i$, on the reactor surface and the emissions from film reflection can be determined from an expression similar to Eqs. 3 and 10, where the diffuse emissions are from all other points on the surface, $\vec{P}_j$, as opposed to a distant light source

$$I_{n,i} = \frac{1}{dA_i} \sum_{S_{\text{Reactor}}} T_{i,j} F_{i,j}\, dA_j E_{n,j}, \tag{16}$$

$$E_{R,n,i} = \frac{1}{dA_i} \sum_{S_{\text{Reactor}}} \left(1 - T_{i,j}\right) F_{i,j}\, dA_j E_{n,j}. \tag{17}$$

Unlike in Eqs. 3, 4, and 10, the close proximity of the receiving and emitting surfaces requires the explicit calculation of the solid angles, $SA_{i,j}$, between the receiving element and all emitting surfaces within the 3-D computational domain

$$F_{i,j} = \frac{\left(\vec{n}_j \cdot \vec{v}_{i-j}\right) SA_{i,j}}{\pi \left|\vec{v}_{i-j}\right|} \tag{18}$$

A methodology of calculating $F_{i,j}$ for 2-D reactor profiles extruded into a third dimension with minimal variations in radiation intensity along the extruded axis has been recently described elsewhere.[13] This methodology was applied here for both $F_{i,j}$ and $T_{i,j}$ for the simulated corrugated reactors, with the understanding that the LASREA at the ends of the corrugated reactor will be overestimated. The effects of this overestimation are quantitatively evaluated within "Results and Discussion" Section. Note that the methodology used is well-suited to long-corrugated geometries where end effects can be neglected, reducing computation times for determining $F_{i,j}$ from hours to seconds by enabling use of the matrix calculation capabilities within MatLAB®.

Repeating this calculation process until the incident energy, $I_{n,i}$, tends to zero leads to the determination of the local energy absorbed due to photon recapture, $q_{R,i}$

$$q_{R,i} = a(\lambda)\left\{I_{1,i} + I_{2,i} + I_{3,i} + \cdots + I_{n,i}\right\}. \tag{19}$$

The total LASREA in the corrugated reactor per W/m^2 lamp emission for a specified $a(\lambda)$ is the sum of $q_{L,i}$ and $q_{R,i}$.

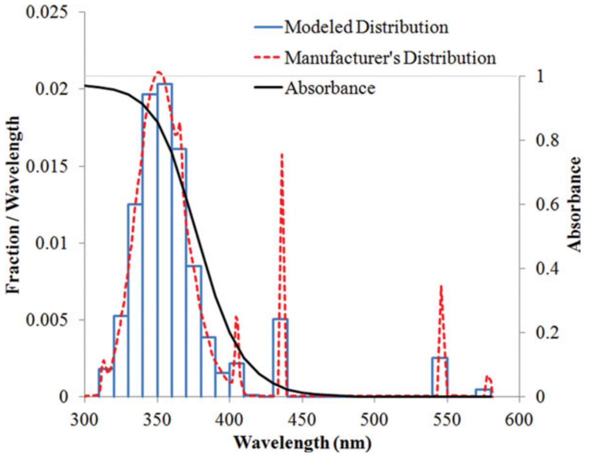

Figure 3. Overlay of the TiO_2 absorption coefficient ($\alpha(\lambda)$) for a 9:1 anatase:rutile composition (Eq. 13) and the emission spectra of the F25T8/BL lamps.

[Color figure can be viewed in the online issue, which is available at wileyonlinelibrary.com.]

MB degradation in the rotating corrugated reactor

Following the experimental determination of k_0 and K_1, the concentration variation within a reservoir located below a rotating corrugated reactor can be calculated provided q_i is known at different reactor rotations. Assuming physical characteristics of the film comparable to those previously described in the tissue absorption method developed by Zhang et al.,[22] the film thickness at a given point on the corrugated surface, δ_i (m), can be expressed as a function of rotations per minute (RPM) and the distance from the center of rotation, r_i (m)

$$\delta_i \times 10^6 = 10.5 + 25.2 \times RPM \times r_i. \tag{20}$$

For an extruded length, $L_\mathrm{e} = 0.2032$ m, the total film volume, V_film, can be calculated as

$$V_\mathrm{film} = L_\mathrm{e} \int\limits_{S_\mathrm{reactor}} \delta_i \, dA_i. \tag{21}$$

The average concentration in the film of the corrugated reactor after a single rotation at a specified RPM, C_degraded (g MB/m^3), for a given inlet film concentration, $C_\mathrm{bulk}|_{t=0}$, can be determined by applying Eqs. 1 and 2 on the discretized surface and solving for the concentration after a full rotation for a temporally varying q_i

$$\frac{dC_{\mathrm{bulk},i}}{dt} = \frac{-k_0 C_{\mathrm{MB},i}}{\left(1 + K_1 C_{\mathrm{MB},i}\right)} \left(\frac{q_i}{q_0}\right)^{0.5} \frac{1}{\delta_i}, \tag{22}$$

$$C_\mathrm{degraded} = \frac{1}{V_\mathrm{film}} \left(\sum_{S_\mathrm{reactor}} C_{\mathrm{bulk},i} L_\mathrm{e} \delta_i dA_i \right)_{t=1/\mathrm{RPM}}. \tag{23}$$

In this work, q_i was modeled for rotations from 0° to 100° (0, 5, 10, 20, …, 100), beyond which the incidence received by the surface was not appreciable. The summation in Eq. 23 was evaluated after the corrugated surface rotated from $-100°$ to $100°$, where the rotation time and duration for each q_i is a function of the RPM. Note that q_i for a negative rotation is a mirror image of its positive counterpart due to the system's symmetry, and that the value of D used in Eqs. 27 and 28 for determining k_0 and K_1 in Eq. 22 is a function of the total MB decomposed in the reservoir.

The degraded film is subsequently submersed into the liquid reservoir where MB diffuses from the reservoir bulk to the film. Consider the reservoir as a perfectly mixed fluid volume, V_r (m^3), through which the corrugated surface with characteristic length equivalent to the length between the corrugation fold and aperture edge passes at its average angular velocity. By applying mass-transfer correlations for liquid flowing above a flat plate[18] to determine the convective mass-transfer coefficient, k [g/(m^2 min)], the replenished film concentration leaving the reservoir, $C_\mathrm{replenished}$ (g MB/m^3), can be explicitly determined for a given submersion time, $t_\mathrm{submerged}$ (min)

$$C_\mathrm{replenished} = C_\mathrm{r} - \left(C_\mathrm{r} - C_\mathrm{degraded}\right) \exp\left[\frac{-kA_\mathrm{film}}{V_\mathrm{film}} t_\mathrm{submerged}\right], \tag{24}$$

where $A_\mathrm{film} = L_\mathrm{e} \int_{S_\mathrm{reactor}} dA_i$ is the surface area of a single corrugation and C_r (g MB/m^3) is the reservoir concentration which is assumed to vary minimally over $t_\mathrm{submerged}$. Note that the submersion time is a function of the fluid reservoir volume and physical configuration, having a value of $t_\mathrm{submerged} = 0.1054/\mathrm{RPM}$ for the experimental system (Figure 1) and varying considerably for even small changes in reservoir height.

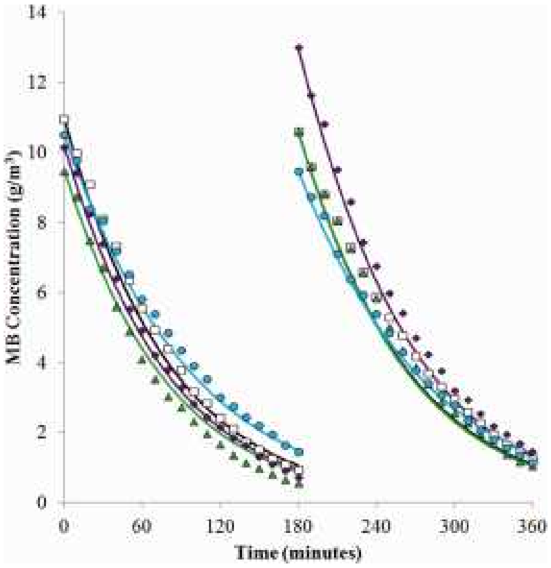

Figure 4. Experimental and predicted flat-plate MB degradation results for 360-min trials (color available via electronic access).

Solid symbols represent two repeated trials with varying initial concentrations (▲, ◆) and a third trial increasing the reservoir volume to 300 mL (●). The open symbols (□) correspond to the first 360 min of the 33 h experiment. [Color figure can be viewed in the online issue, which is available at wileyonlinelibrary.com.]

Equating $C_\mathrm{bulk}|_{t=0}$ to $C_\mathrm{replenished}$ and iteratively solving Eqs. 22 and 24 for a converged C_degraded yields the replenished and degraded film concentrations resulting from mass-transfer limitations between the reservoir and film surface during submersion. The temporal variation of reservoir concentration can thus be determined from a mass balance

$$\frac{dC_\mathrm{r}}{dt} = \frac{\left(C_\mathrm{degraded} - C_\mathrm{replenished}\right) V_\mathrm{film} N_\mathrm{c} \mathrm{RPM}}{V_\mathrm{r}}. \tag{25}$$

Flat-Plate Results and Discussion

Light source characterization and model validation

Defining the point on the counter centered below the lamp array as the origin with the z-axis corresponding to the extrusion axis in Figure 1 and the y-axis corresponding to the height, UV measurements were obtained at three positions ($x = 0$; $y = 22$ cm; $z = -6.2$, 4, and 14 cm). Both direct incidence from the lamp and diffuse incidence from photos reflected by the light box and work surface were considered. Combined direct and diffuse incidence were measured at each position by orienting the sensor toward the lamp array, while diffuse-only incidence was determined by orienting the sensor toward the counter (i.e., limiting direct incidence from the lamp). Based on the spectral distribution provided by the lamp manufacturer (Figure 3) and the 360–370 nm wavelength sensitivity of the UV sensor, the total measured incidence accounted for approximately 16.2% of the incidence from the lamp's full spectrum.

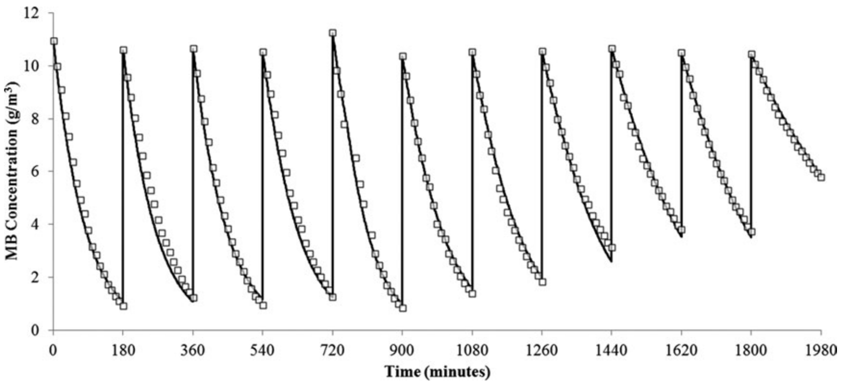

Figure 5. Experimental and predicted flat-plate MB degradation results for an extended 33 h experiment.

The diffuse measurement remained fairly constant at 2 W/m^2, corresponding to a total diffuse incidence across all wavelengths of 12.35 W/m^2. The combined direct/diffuse measurements at $z = -6.2$, 4, and 14 cm were 44.7, 45.2, and 41.4 W/m^2, respectively. Removing the diffuse contribution and correcting for the sensor's band-gap yield total direct incidence values of 263.6, 266.6, and 243.2 W/m^2, respectively. Dividing by the total lamp emission rate (693.75 W/m^2) yields I_i/W_{light} values of 0.380, 0.384, and 0.351, respectively. The I_i/W_{light} predicted at these locations was 0.381, 0.385, and 0.348, exhibiting remarkable agreement considering the potential experimental error due to uncertainty in sensor positioning, sensitivity, accuracy ($\pm 2\%$), and actual lamp emission rates. Due to the limited contribution of diffuse incidence ($<5\%$) and the subsequent reductions that would arise when the reactors were placed within the radiation field, only direct incidence was considered in subsequent derivation of kinetics and reactor modeling.

MB degradation on a flat plate

A series of three short experiments (360 min; Figure 4) and one extended experiment (33 h; Figure 5) were performed to quantify k_0, K_1, and their dependence on catalyst deactivation and total MB decomposed. At 180 min intervals during each run, the flat plate was temporarily removed from the beaker and the degraded MB solution replaced with 250 mL of fresh solution. The resulting set of $\sim$380 data points (10 min sampling interval) was used to determine the rate of MB decomposition for varying initial bulk solution concentrations and cumulative grams MB decomposed per unit surface area during each run, D (g MB/m^2)

$$\frac{dC_{\text{bulk}}}{dt} = \frac{-k_0 C_{\text{MB}}}{(1 + K_1 C_{\text{MB}})} \left(\frac{q}{q_0}\right)^{0.5} \frac{\pi d_{\text{plate}}^2}{4V_{\text{r}}}. \tag{26}$$

For a simulated average flat-plate LASREA of $q = 197.25$ W/m^2, the following relationship was obtained for the fitted parameters in Eqs. 1, 22, and 26

$$k_0 = 3.3553 \times 10^{-4} - 4.9187 \times 10^{-5} D - 4.0422 \times 10^{-6} D^2, \tag{27}$$

$$K_1 = 0.3419 + 3.8634 \times 10^{-2} D - 1.1219 \times 10^{-5} D^2. \tag{28}$$

The MB concentrations predicted by Eqs. 26–28 for each of the trials are shown as solid lines in Figures 4 and 5. Note that in one of the 360 min experiments (● in Figure 4) and at 1640 min in Figure 5, the volume of solution added was 300 mL. This resulted in the observed deviation in behavior relative to the other trials (250 mL) and was accounted for in the data regression and model predictions by increasing V_{r} for the appropriate periods. By the end of the 360 min and 33 h experiments, the value of D approached 0.93 and 4.3 g MB/m^2, respectively.

Corrugated Reactor Results and Discussion

Incidence, LASREA, and validation of assumptions

Using the emission spectra and absorption coefficients depicted in Figure 3, the final (net) LASREA distributions at different clockwise rotations were determined by calculating the incidence and reflectance at the surface for each orientation, determining the LASREA profiles for arbitrary TiO$_2$ absorption coefficients and performing an emission-spectra-weighted summation of these profiles to yield the net LASREA distribution on the reactor surface at different clockwise rotations.

The use of an average lamp incidence and reflectance (light reflected by the liquid surface) along the extruded reactor length was supported by a maximum observed deviation of 3.5% in dry and wet incidence and reflectance (Figure 6), with the liquid film significantly reducing the incidence relative to that of a dry surface. Illustrative profiles of

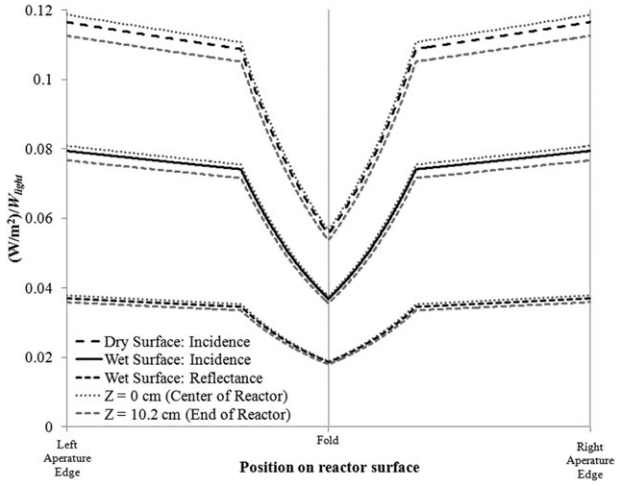

Figure 6. Simulated (z = 0 and 10.2 cm) and averaged incidence and reflectance distributions of the experimental configuration oriented at a clockwise rotation of 0° under both dry and wetted conditions.

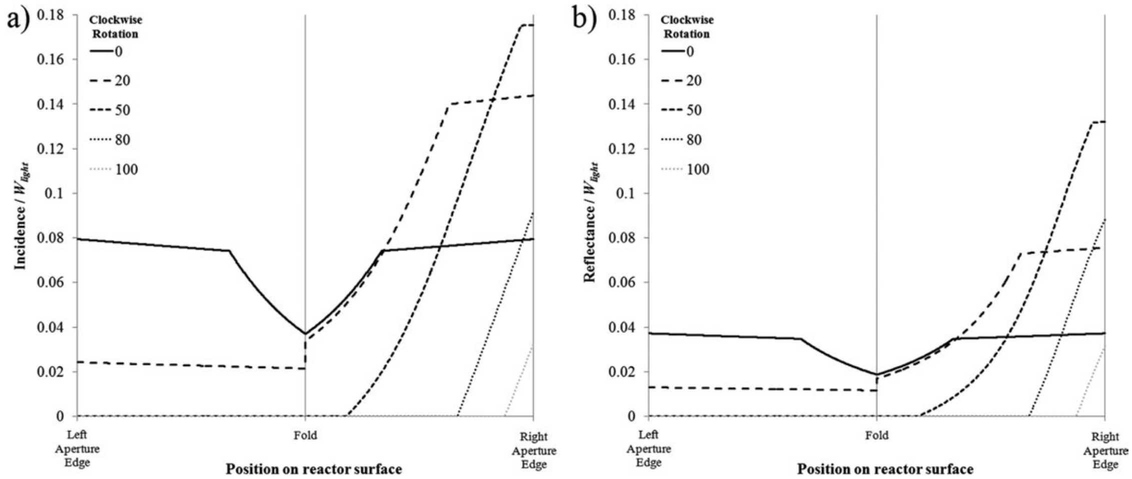

Figure 7. Averaged incidence (a) and reflectance (b) of the reactor depicted in Figure 1 at clockwise rotations ranging from 0° to 100° for wetted conditions.

average incidence and reflectance for clockwise rotations ranging from 0° to 100° are depicted in Figure 7. The LASREA for arbitrary $a(\lambda)$ ranging from 0.1 to 1.0 was subsequently determined at each rotation. Typical results are provided in Figure 8 for a single clockwise rotation (0°) and four values of $a(\lambda)$, illustrating the increased impact of $a(\lambda)$ on photon recapture near the aperture fold relative to regions near the aperture edge. Using the emission spectra (W_{light}) and TiO_2 absorption coefficient of the experimental system (Figure 3), the final LASREA, q_i, at each clockwise rotation was determined (Figure 9).

One of the key assumptions made in determining q_i was that the geometry extended for an appreciable distance along both the positive and negative z-axis. Although applicable at the center of the corrugated reactor (i.e., $z = 0$ cm), this assumption is clearly invalid at each of the reactor's ends ($z = \pm 10.2$ cm). The calculated q_i for a reactor extruding in only the positive z-axis (Figure 10) indicates that reduced photon recapture at the edge of the reactor results in 13–7% lower total energy absorbed for low to high rotations, respectively. Although appreciable, this reduction in LASREA is limited to the very edges of the reactor. The impact of this reduction is further mitigated by the square-root dependence of the degradation kinetics on q_i and is thus neglected for subsequent modeling of MB degradation in the rotating corrugated reactor system.

Comparison to experimental MB degradation

The temporal variation in MB concentration within the reactor reservoir was measured for rotation rates of 9, 15, and 30 RPM and compared to those predicted using the flat-plate reaction kinetics and simulated LASREA profiles (Figure 11). The simulated degradation rate of MB in the reservoir was consistent with that observed experimentally, albeit with increasing variation at higher rotation rates and extended runtimes. These deviations were attributed to two effects: bubble formation on the surface of the reactor at higher RPMs and reduced submersion times in the reservoir as sampling was conducted for absorbance measurements.

During the experiments, bubbles would often form on the surface of the reactor as it disengaged from the reservoir (Figure 12). At lower rotation rates, the bubble film had sufficient time to drain and burst prior to the corrugation reaching its apex. At higher rotation rates, the bubble film frequently remained intact throughout the rotation of the corrugation, potentially reflecting photons away from the reactor

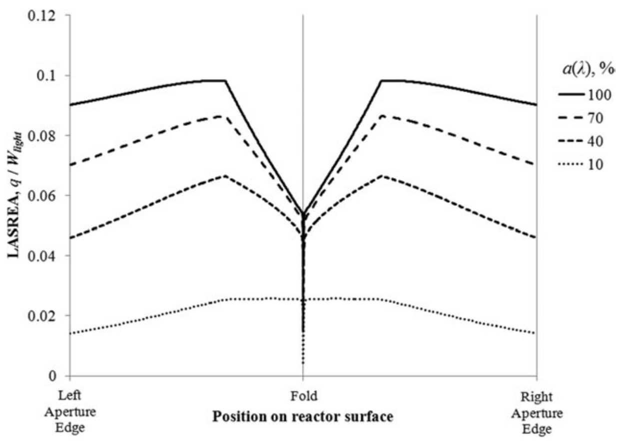

Figure 8. LASREA of the reactor depicted in Figure 1 for a clockwise rotation of 0°, wetted conditions, and arbitrary absorption coefficients, $a(\lambda)$, ranging from 0.1 to 1.

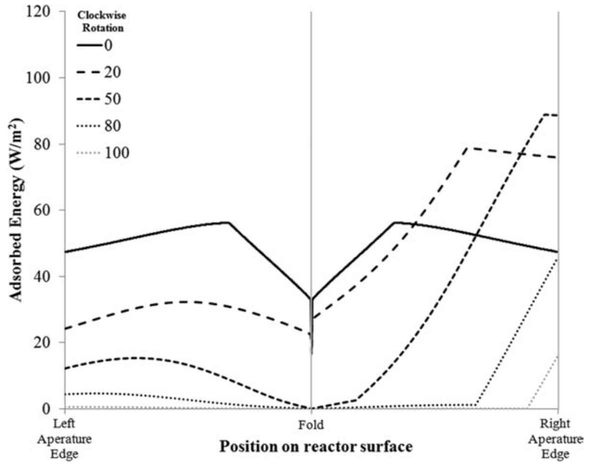

Figure 9. Total energy absorbed, q_i, for the geometry depicted in Figure 1 and spectra in Figure 3, extruded along both the positive and negative z-axis.

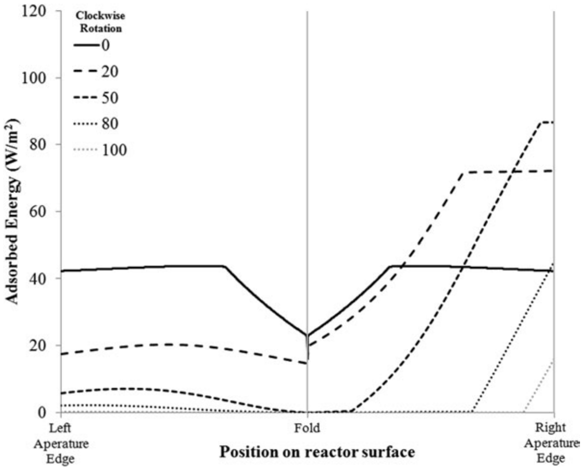

Figure 10. Total energy absorbed at the edge of the geometry depicted in Figure 1 (i.e., photon recapture from an extruded geometry in the positive *z*-axis only).

surface and reducing the active area for MB degradation. The impact of the bubbles on the total MB decomposed within a single rotation is a complex function of the bubble's position within the corrugation, its persistence, its impact on the radiation profile on the surface contained within the bubble, and the liquid film thickness remaining on the surface below the bubble. Although the observed fit between experimental and simulated results could be improved through an empirically based modification of the active film surface area and volume, V_{film}, such a modification would have limited utility beyond this study. Instead, we note the increasing impact of these bubbles on experimental results at higher rotation rates, limiting the extent to which the current computational model can be relied upon to describe experimental performance beyond 30 RPM.

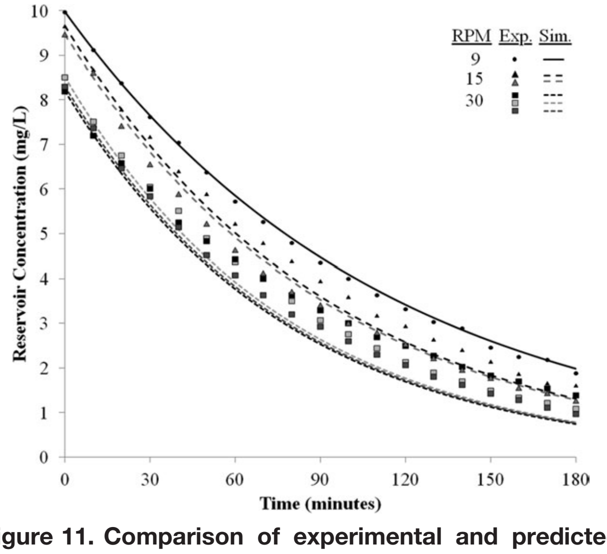

Figure 11. Comparison of experimental and predicted corrugated reactor performance for MB degradation.

Color variations of 15 and 30 RPM results represent repeated experiments with differing initial MB concentrations.

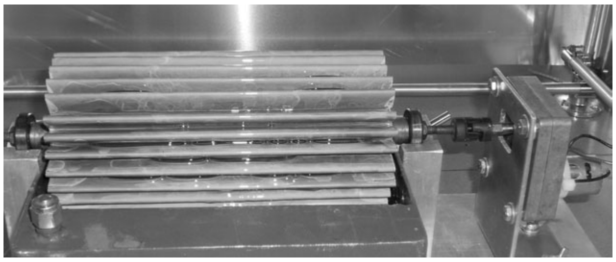

Figure 12. Bubble formation on a noncoated corrugated reactor surface rotating at 15 RPM.

Preliminary attempts to simulate this system assumed no mass-transfer limitations between the corrugated surface and reactor, resulting in significant overestimation of the degradation rate of MB in the reservoir. The current model simulates reservoir-to-surface mass transfer using flat-plate correlations from the literature[18] and a single adjustable parameter, $t_{\text{submerged}}$, which is a function of the fluid volume in the reservoir, V_r, the cross-sectional area of the reservoir base, A_r, the height of the center of rotation of the corrugated reactor above the base of the reservoir, h_C, and the reactor geometry

$$t_{\text{submerged}} = \frac{1}{\pi \text{RPM}} \arccos\left(\frac{h_C}{r_{\text{avg}}} - \frac{V_r - V_{\text{film}} N_c - 6.334 \times 10^{-5}}{A_r r_{\text{avg}}}\right). \tag{29}$$

For the configuration depicted in Figure 1, the mid-point radius of the corrugated geometry was r_{avg} (m) $= 0.032 + \text{depth}/2 = 0.0416$, A_r (m^2) $= 0.03242$ (based on 6″ × 8.375″), and h_C (m) $= 0.07435 \pm 0.0005$. The terms subtracted from V_r represent the film liquid volume from Eq. 21 and the measured recirculation loop volume (2 m of 6.35 mm ID tubing). Note that there is additional uncertainty in Eq. 29, as the volume displaced by the submersed reactor would increase the apparent V_r (increasing $t_{\text{submerged}}$) while excess fluid carried up from the reactor surface would decrease the apparent V_r (decreasing $t_{\text{submerged}}$). The relative impact of displacement and excess fluid entrainment was assumed comparable and, thus, neglected.

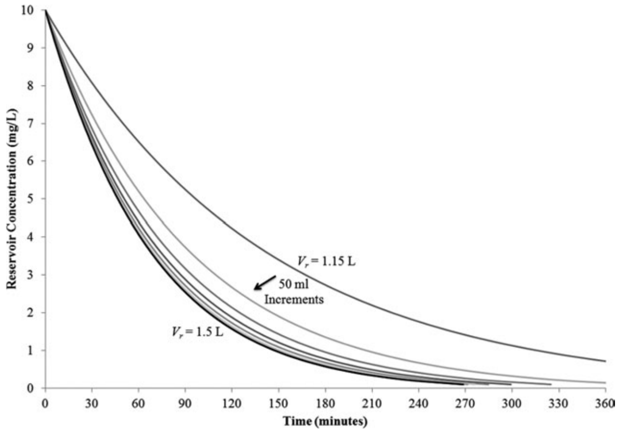

Figure 13. MB concentration profile for increasing reservoir volumes. Reservoir to reactor mass transfer limits MB degradation at low V_r, with significant performance improvements as V_r (and $t_{\text{submerged}}$) increase.

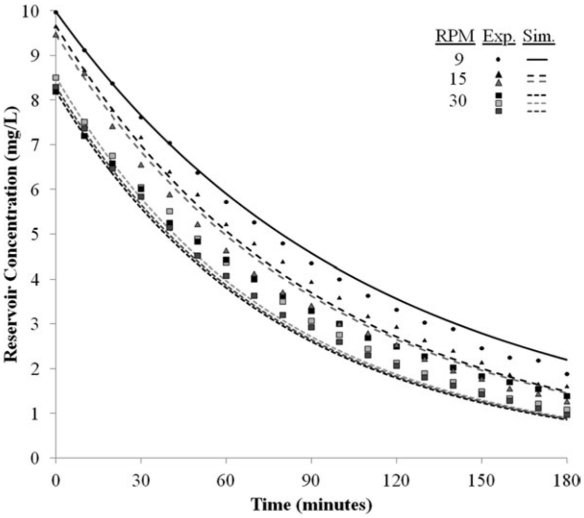

Figure 14. Comparison of experimental and predicted corrugated reactor performance when sample volumes of 2 mL are deducted from V_r at 15-min intervals.

The resulting impact of accounting for mass-transfer limitations for varying contact times is significant (Figure 13), where arbitrary selection of V_r and $t_{submerged}$ could potentially produce the observed agreement with experimental data in Figure 11. It is for this reason that the calculation methodology for $t_{submerged}$ has been described in such detail, and a value of $V_r = 0.0012$ m^3 used exclusively in deriving the results in Figure 11. Because of the sensitivity of the reservoir concentration on reactor volume, additional simulations were repeated while accounting for the removal of 2 mL of reservoir volume every 15 min for sampling (Figure 14). The decrease in $t_{submerged}$ from a reduced V_r had an appreciable effect at later runtimes relative to Figure 11, signifying the need for rigorous tracking of fluid volumes during experimentation. Additional experiments beyond those performed in this study are needed to validate the flat-plate correlations used for reservoir to film mass transfer and the simulated impact of increasing V_r on MB concentration within the reservoir.

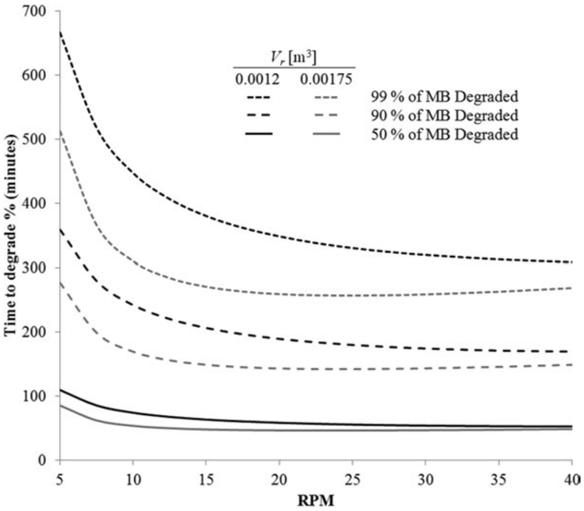

Figure 15. Impact of rotation rate on the time needed to decompose 50, 90, and 99% of MB in solution for the geometry depicted in Figure 1 and reservoir volumes of 1.2 (mass-transfer limited) and 1.75 L (extended $t_{submerged}$).

Parametric analysis and reactor optimization

Two case studies were performed for the current system (base case) and an initial MB reservoir concentration of 10 g/m^3: varying RPM to balance single-pass decomposition against reservoir-to-film mass transfer and varying the active area of the geometry away from the base case by either increasing the corrugation depth for a set N_c or increasing N_c for a set depth.

Increased rotation rates of the corrugated geometry have a proportional effect on V_{film} due to Eq. 20 and an inverse effect on single pass MB decomposition due to the reduced rotation time and submersion time. For $V_r = 0.0012$ m^3, increasing the RPM above 10–15 RPM had a negligible effect on the time required to decompose half of the MB in solution (Figure 15). Even at greater decomposed fractions, increasing the rotation rate beyond 15 RPM had a marginal effect on the time needed for decomposition. When mass-transfer limitations between the film and reservoir were relaxed ($V_r = 0.00175$ m^3 in Figure 15), the performance at higher rotation rates actually decreased due to reduced UV degradation relative to the MB transferred from the reservoir. Considering the experimentally observed increase in bubble formation and persistence relative to rotation period at higher rotation rates, the time required to reach a given percentage degradation in Figure 15 for elevated rotation rates is likely an underestimate.

The second case study explored the relative impact of two strategies for varying the active surface area in a corrugated geometry: increasing the depth or increasing the number of corrugations. To improve comparability of the results for different corrugation depths, $t_{submerged}$ was set at 0.007 min (corresponding to $V_r = 0.0012$ m^3 for the base case geometry operating at 15 RPM). For each of the four alternative geometries considered (Table 1), the incident energy profile, LASREA, total absorbed energy, and reactor performance were calculated at different rotation rates. The resulting reservoir concentration profile at 15 RPM (Figure 16) was found to be reflective of the general behavior observed for the different geometries. For a constant distance of 3.2 cm between the corrugation fold and center of rotation, changes to the number of rotations had a significantly greater impact on overall reactor performance than changes to the corrugation depth for a given surface area. For the flat-plate mass-transfer correlations used,[18] k decreases for increasing fold-to-aperture lengths. As significant mass-transfer limitations already exist for the base case when $V_r = 0.0012$ m^3, it is advantageous to increase the surface area of a given corrugated reactor by increasing the number of corrugations (thereby decreasing the corrugation half-angle and fold-to-

Table 1. Characteristic Parameters of Geometries Considered in the Second Case Study*

Geometry	Area (cm^2)	Half Angle (°)	Depth (cm)	N_c
Base case	2308	16.5	1.95	28
Case 1	1150	27.0	0.90	28
Case 2	1150	34.4	1.95	12
Case 3	4632	11.4	3.99	28
Case 4	4632	8.14	1.95	58

*Note that the fold to center of rotation distance remained constant at 3.2 cm. Extrusion length = 20.32 cm.

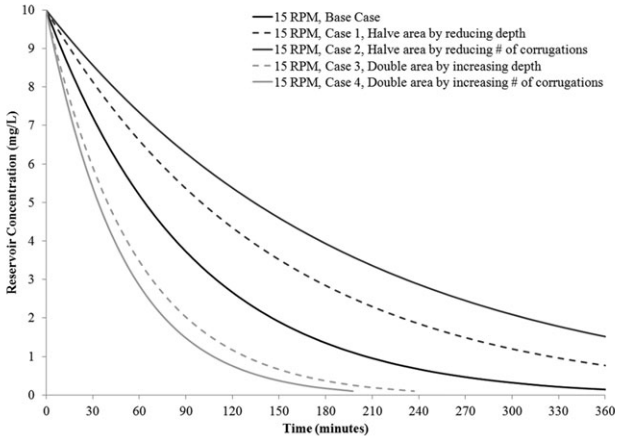

Figure 16. Reactor performance for different active areas achieved by varying the number and depth of corrugations as per Table 1.

aperture-edge distance). There are, however, practical limitations on the number of corrugations and aperture width due to increased bubble formation and persistence as the aperture width decreases.

The majority of stable bubbles formed in the experimental system were located in the fold region of the reactor (Figure 12), where reduced capillary forces acting on the bubble film results in longer drainage times and increased bubble persistence. If the reactor area were increased by increasing the number of corrugations, the half-angle would be significantly reduced relative to the base-case system. It is reasonable to assume that the bubble interface would be stable at locations farther away from the fold, potentially resulting in a significant reduction in active area and overall reactor performance. In contrast, increasing the corrugation depth at a constant 3.2 cm fold to center of rotation distance would have a reduced impact on the corrugation half-angle, significantly decreasing the area over which bubbles are likely to form. This suggests that, in the absence of a method for actively breaking bubbles, the number of corrugations and corrugation depth can be optimized to minimize the impact of bubble formation on reactor performance via geometric modifications alone.

Summary and Future Work

The experimental and computational analysis of flat plate and rotating corrugated reactor performance have been discussed for the TiO_2 catalyzed decomposition of MB. The derived kinetic expressions describe the dependence of MB decomposition rates on both the local radiation absorption and the extent of catalyst deactivation, enabling subsequent computational analysis of the rotating reactor system. By simulating the transient LASREA and determining MB decomposition during a single rotation for varying inlet film concentrations, the corrugated reactor was decoupled from the fluid reservoir which could then be modeled using a mass balance and flat-plate mass-transfer correlations. The simulated result was consistent with experimental observations with deviations arising from bubble formation on the corrugated surface, reservoir volume variations, and inherent limits on experimental accuracy. Parametric analysis indicates that rotation rates on the order of 15 RPM are appropriate for optimal MB degradation, with the V_r and $t_{\text{submerged}}$ having a significant effect on overall system performance due to mass-transfer limitations between the rotating corrugated reactor and fluid reservoir. Future work will explore the effect of rotation rate and geometry on bubble formation and mass transfer, validating the assumed mass-transfer correlations and experimentally confirming the observed sensitivity of MB degradation on V_r.

Notation

$a(\lambda)$ = spectral absorption coefficient of the TiO_2 film
A_{film} = surface area of a single corrugation
C_{bulk} = concentration of MB in the bulk
C_{degraded} = degraded film concentration after one rotation
C_{MB} = concentration of MB at the catalyst surface
C_r = MB concentration in the fluid reservoir of the corrugated reactor
$C_{\text{replenished}}$ = replenished film concentration after submersion
dA_i = area of receiving surface i
dA_j = area of emitting surface j
d_{plate} = diameter of flat plate
D = g/m^2 MB degraded by the catalyst surface
D_{MB} = diffusifity of MB in water
$E_{n,j}$ = emission rate from surface j after the nth reflection
$E_{\text{R},n,j}$ = diffuse reflections from liquid film on surface j after the nth reflection
$F_{i,j}$ = emission factor for surface j emitting to surface i
I_i = local area-specific energy incidence received on surface I, W/m^2
$I_{n,i}$ = incidence on surface i from $E_{n,j}$
k = flat-plate mass-transfer coefficient, g/(m^2 min)
k_0 = rate equation coefficient
K_1 = rate equation coefficient
L_e = Z-axis extrusion length of the corrugation
$\vec{n}_i$ = unit normal of receiving element i
$\vec{n}_j$ = unit normal of emitting element j
N_c = number of corrugations
$\vec{P}_i$ = vector coordinates of point i
$\vec{P}_j$ = vector coordinates of point j
q = surface-averaged LASREA for flat plate
q_i = LASREA at point i
$q_{\text{L},i}$ = LASREA at point i from lamp emissions
$q_{\text{R},i}$ = LASREA at point i from photon recapture
q_0 = reference LASREA (1 W/m^2)
r_i = distance between point i and center of rotation
r_{mb} = generation rate of MB
$SA_{i,j}$ = solid angle between emitting surface j and receiving surface i
S_{Light} = surface domain of emitting light source
t = time
$t_{\text{submerged}}$ = submersion time
$T_{i,j}$ = transmittance factor surface i receiving light from surface j
$\vec{v}_{i-j}$ = vector from center of surface j to center of surface i
V_{film} = integrated film volume on a single corrugation
V_r = volume of fluid reservoir
W_{light} = specific emission rate of lamp
x, y, z = spatial coordinates of point
δ = diffusion boundary layer thickness
δ_i = thickness of the film at point i
λ = wavelength

Literature Cited

1. Matthews RW. Photooxidation of organic impurities in water using thin films of titanium dioxide. *J Phys Chem*. 1987;91:3328.
2. Cassano AE, Martin CA, Brandi RJ, Alfano OM. Photoreactor analysis and design: fundamentals and application. *Ind Eng Chem Res*. 1995;34:2155–2201.
3. Spadoni G, Bandini E, Santarelli F. Scattering effects in photo-sensitized reactions. *Chem Eng Sci*. 1978;33:517.
4. Yokota T, Cesur S, Suzuki H, Baba H, Takahata Y. Anisotropic scattering model for estimation of light absorption rates in photoreactor with heterogeneous medium. *J Chem Eng*. 1999;32:314.
5. Romero RL, Alfano OM, Cassano AE. Cylindrical photocatalytic reactors. Radiation absorption and scattering effects produced by suspended fine particles in an annular space. *Ind Eng Chem Res*. 1997;36:3094–3109.

6. Sgalari G, Camera-Roda G, Santarelli F. “Discrete ordinary method in the analysis of radiative transfer in photocatalytically reacting media. *Int Commun Heat Mass Transfer*. 1998;25:651.
7. Chui EH, Raithby GD. Computation of radiant heat transfer on a non-orthogonal mesh using the finite-volume method. *Numer Heat Transfer B*. 1993;23:269.
8. Pareek VK, Adesina AA. Light intensity distribution in a photocatalytic reactor using finite volume. *AIChE J*. 2004;50:1273–1288.
9. Donaldson AA, Zhang Z. UV absorption by TiO_2 films in photocatalytic reactors: effect of fold curvature. *AIChE J*. 2012;58:1578–1587.
10. Zhang Z, Anderson WA, Moo-Young M. Radiation modeling of air phase corrugated plate photocatalytic reactor. *Dyn Continuous Discrete Imulsive Syst Ser B Appl Algorithms*. 2004;11:59–68.
11. Shang H, Zhang Z, Anderson WA. Non-uniform radiation modeling of a corrugated plate photocatalytic reactor. *AIChE J*. 2005;51:2024–2033.
12. Zhang Z, Anderson WA, Moo-Young M. An engineering model for the scale-up and design of photocatalytic reactors. *Int J Chem Reactor Eng*. 2003;1:A57.
13. Donaldson AA, Zhang Z. Coupled transport phenomena in corrugated photocatalytic reactors. *Chin J Chem Eng*. 2011;19:763–772.
14. Meunier SM, Gamage J, Duvnjak Z, Zhang Z. Design and characterization of a novel rotating corrugated drum reactor for wastewater treatment. *Int J Photoenergy*. 2010;2010:10.
15. Tschirch J, Dillert R, Bahnemann D, Proft B, Biedermann A, Goer B. Photodegradation of methylene blue in water, a standard method to determine the activity of photocatalytic coatings. *Res Chem Intermed*. 2008;34:381–392.
16. Zhang Z. Analysis of a corrugated plate photocatalytic reactor. PhD Thesis, Waterloo, Ontario, Canada: University of Waterloo, 1999.
17. Zhang Z, Anderson WA, Moo-Young M. Modeling of corrugated plate photocatalytic reactors and experimental validation. *Chem Eng Sci*. 2003;58:911–914.
18. Litt M, Friedlander SK. An experimental study of diffusion-controlled reactions in a laminar boundary layer. *AIChE J*. 1959;5:483–485.
19. Crittenden JC, Zhang Y, Hand DW, Perram DL. Destruction of organic compounds in water use supported photocatalysis. *J Solar Energy Eng*. 1996;118:123.
20. Hamal DB. Design and development of a new generation of UV-visible-light-driven nanosized codoped titanium dioxide photocatalysts and biocides/sporocides, and environmental applications. PhD Thesis, Manhattan, Kansas: Kansas State University, 2009.
21. Tayade RJ, Surolia PK, Kulkarni RG, Jasra RV. Photocatalytic degradation of dyes and organic contaminants in water using nanocrystalline anatase and rutile TiO_2. *Sci Techol Adv Mater*. 2007;8:455–462.
22. Zhang L, Anderson WA, Zhang Z. Development and modeling of a rotating disc photocatalytic reactor for wastewater treatment. *Chem Eng J*. 2006;121):125–134.

Manuscript received Nov. 30, 2011, and revision received Apr. 20, 2012.